Elastic response of polymer-nanoparticle composite sponges: Microscopic model for large deformations

Anish Sukumar[1], Nirmalya Bachhar[1,2,*], Apratim Chatterji[3,†] and Guruswamy Kumaraswamy[1]

[1]*Department of Chemical Engineering, Indian Institute of Technology Bombay, Powai, Mumbai 400076, India*
[2]*Department of Chemical Engineering, Indian Institute of Technology Jodhpur, Rajasthan 342037, India*
[3]*Department of Physics, Indian Institute of Science Education and Research (IISER-Pune), Pune 411008, India*

We propose a minimalist coarse-grained microscopic model to investigate the mechanical response of ice-templated polymer nanocomposite sponges with large open voids. Earlier experimental work [Rajamanickam *et al.*, Chem. Mater. **26**, 5161 (2014)] has demonstrated that such systems show elastic recovery after being subjected to large compressive strains exceeding 80%, despite being comprised primarily of inorganic nanoparticles. Our model captures the essential features of the nonlinear mechanical response to uniaxial compression up to strain $\gamma = 0.8$. From our simulation we identify three different regimes for the stress response: (i) the stress increases linearly with strain at low strains up to ≈ 0.2; (ii) at intermediate strains, such that γ is approximately in the range $0.2 - 0.5$, we observe a plateau regime in the stress-strain data; and (iii) finally we see a sharp increase in stress at strains >0.5. This agrees with experimental observations. The model helps us establish a correlation between the stress-strain response and the underlying microscopic reorganization of microstructure spanning multiple length scales, which leads to the emergence of the three regimes. The nature of individual void deformations was statistically analysed to demonstrate the progression of void shapes as the sponge is compressed. We also establish that nanoparticles at the interface of voids respond differently to stress as compared to those away from the interface. Our simulation model is versatile and allows us to vary parameters, which correspond to variations in the cross-link density and architecture of nanoparticle connectivity in experiments.

I. INTRODUCTION

In the recent decades, there has been increasing interest in nanoparticle polymer composites due to their technological applications. Typically, polymer nanocomposites refer to systems where a small fraction of nanofiller such as nanoclay [1], carbon nanotubes [2], or graphene [3] is added to a polymer matrix to enhance functional properties [4,5] such as stiffness, thermal properties, permeability, etc. Another class of polymer nanocomposites are materials where the fraction of the rigid inorganic phase predominates, and the polymer functions as a binder. Examples of such materials are observed in nature, e.g., nacre [6], as well as in nature-inspired synthetic analogues [7,8]. Given the wide technological ramifications of polymer nanocomposites, their science and engineering have been widely investigated by researchers drawn from different disciplines [1–5,9–25].

We are particularly interested in the mechanical properties of porous polymer nanocomposites. Ultralight porous aerogels that combine low nominal density with mechanical rigidity find use in applications in industrial insulation, as catalyst supports, as well as in aerospace components [26]. The balance of properties in such aerogels is realized by carefully engineering their architecture [27–31]. Porous aerogels whose walls are comprised of polymer nanocomposites can be prepared using ice templating [32–35]. Such materials show potential for several applications such as fire retardant foams [36], sponges capable of absorbing liquids with different polarities [37], high-surface area monoliths for catalytic reactions [38], as flexible capacitors [39] as well as for use in artificial tissues with biomedical relevance [40].

Recently, we have reported the preparation of porous ice-templated polymer nanoparticle nanocomposites wherein the polymer matrix is cross linked in the frozen state [41]. Inorganic nanoparticles (NPs), polymers, and cross-linker molecules are dispersed in water and the dilute aqueous system is frozen such that large ice crystals form that are several tens of microns in size. The NPs, polymers, and cross linker are expelled from the crystals and aggregate between domains of ice crystals to form thin interconnected domain walls that are microns thick. Polymers within the walls get cross linked in the frozen state enmeshing the NPs, and subsequently when the ice crystals are removed at higher temperatures, the NP and polymer mixture are organized to form a self-standing sponge. The sponge is characterized by a porous percolating structure of the NP-polymer mesh surrounding interconnected voids. Sponges that are centimetres in size can be readily prepared using this method. We refer the reader to a schematic in Fig. 1(a) explaining the preparation method and SEM images of the nanocomposite sponge in Figs. 1(b) and 1(c). We can

*Corresponding author: nirmalya@iitj.ac.in
†Corresponding author: apratim@iiserpune.ac.in
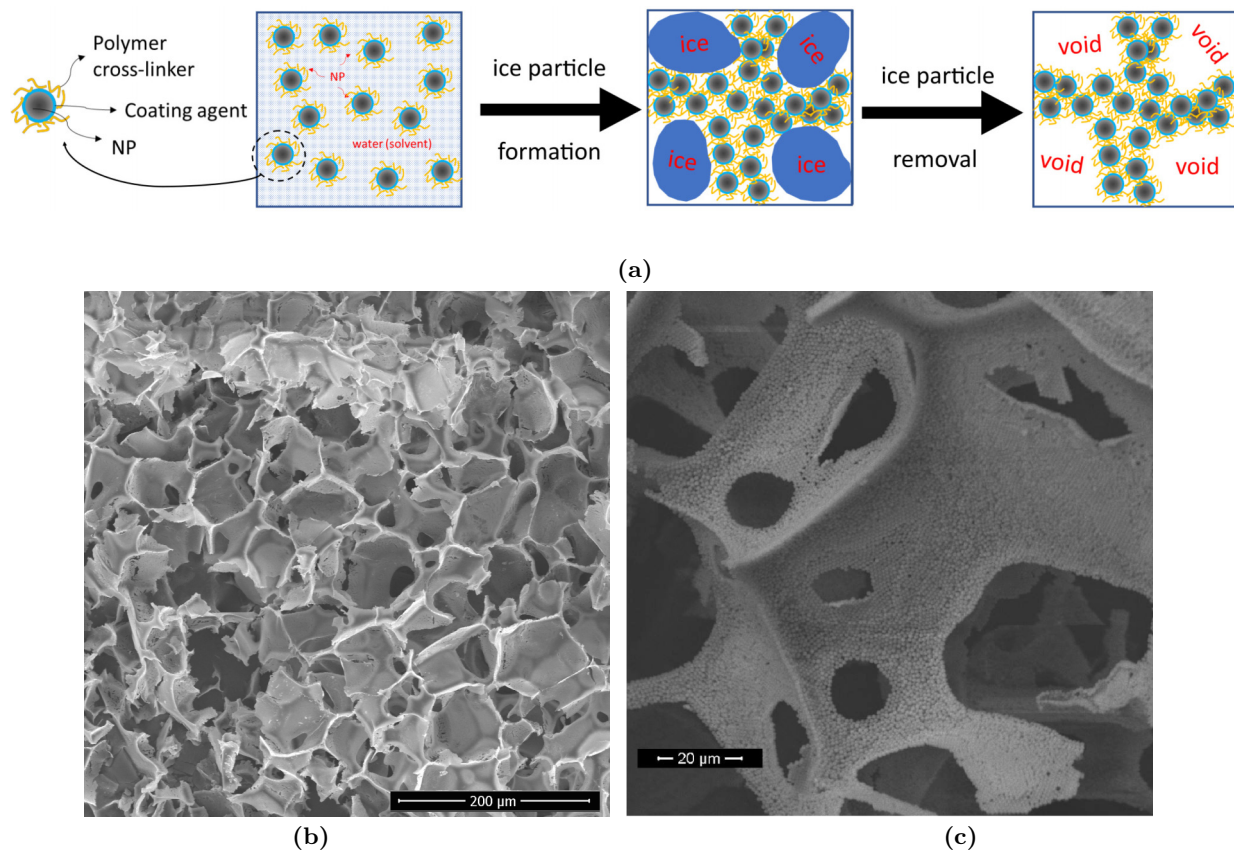
(a)

(b)

(c)

FIG. 1. (a) A schematic description of how the inorganic sponge is prepared in the laboratory. The left box shows the polymer coated nanoparticles (NPs), which are dispersed in water. The middle box shows the solution after it is frozen to form ice crystals such that the NP, polymer, and cross linker are expelled from frozen crystals and occupy the gaps between ice crystals. The polymer is then cross linked to create a mesh in which the NPs are enmeshed. The right box schematically shows that the NPs remain enmeshed in the polymeric gel when the ice crystals are removed and form polymer-nanocomposite surfaces surrounding empty voids. (b) SEM images of the experimental system taken from Rajamanickam *et al.* [41], where we can see the internal structure of the scaffolds. The scale bar is 200 μm. (c) The zoomed in (scale bar 20 μm) structures where individual NPs are visible. The subfigure also shows that the void walls consist of multiple openings and thereby the walls form a scaffold with open voids. The computational model describing the system is shown in Fig. 2.

see the nanocomposite walls surrounding the voids, as well as the individual NPs by zooming into the figures. The polymeric mesh is only a few nanometer in thickness and cannot be visualized using electron microscopy. The major component of these sponges is the inorganic NPs, up to 90% by weight, with the cross-linked polymer comprising the remaining 10%. Despite the high loading of NPs, the sponges tolerate large compressive strains (up to 90%) and recover when the compressive force is released [41]. At low strains, the sponge modulus varies linearly with the nominal density. The mechanical response of these sponges is nonlinear. A plateau region is observed beyond the low-strain linear regime, and at significantly higher strains, the stress increases rapidly. Such flexible ice-templated nanocomposite sponges are platform materials with wide-ranging applications [36,37,39,42].

The mechanical response of ice-templated nanocomposite sponges may be attributed to their microstructure [43]. Typically, cationic amine-containing polymers are used, that adsorb on anionic inorganic NPs in aqueous solutions. Excess polymer and cross linker are confined to the inter-NP spaces in the walls of ice crystals and get cross linked on holding the system in the frozen state. Therefore, on removal of the

ice crystals, the walls of the sponge comprise of NPs that are enmeshed in a cross-linked polymer network. The NPs are not covalently bonded to the polymers—rather, the polymers adsorb on the NP surface. The NPs are trapped in the cross-linked mesh that responds when the sponge is compressed. Therefore, these sponges are soft, with moduli $\sim O(10^4$ Pa), despite their high inorganic NP content.

Here we propose a microscopic coarse-grained model to describe the mechanical response of ice-templated nanocomposite sponges, which works remarkably well to capture the macroscopic behavior of the system, despite many simplifying assumptions. A complete molecular description of the true hierarchical microstructure of the sponge is clearly intractable. In one experimental realization, the $\sim O(1)$-cm porous sponge comprises 22 nm silica NPs in a cross-linked polyethyleneimine network forming $\sim O(10 \, \mu$m) walls that surround $\sim O(100 \, \mu$m) pores. Continuum solid mechanical descriptions of the mechanical response of open foam structures are available [44], as are molecular models for polymer nanocomposites [45–48]. However, researchers have previously not attempted to rationalize the macroscopic mechanical response of an open-cell sponge starting from a *microscopic*

description of the nanocomposite structure in the walls, especially because of the challenges of incorporating the physics at multiple length scales. Thus, coming up with a viable model, which can be handled computationally, and also effectively captures the stress-strain response of the inorganic sponge is the focus of the present paper.

To render the problem tractable, we work with an idealized system where the sponge walls are represented by a network of spherical beads (representing the NPs) interconnected with its neighboring beads by massless springs. The springs represent the entropic elasticity of the polymer-gel network that encapsulates the NPs. This bead spring network has large voids in its midst, akin to the experimental system. To simplify, we assume that all the voids in the as prepared sponge are of the same size and shape (spherical). Moreover, we try to minimize fluctuations in the mesh thickness. As we establish in this paper, the polymer degrees of freedom of the system can be coarse grained out to have a simpler model. This coarse-grained model, without the explicit modeling of the polymer, reproduces the stress-strain behavior of the experimental systems. Moreover, it provides quantitative insights into the microscopic dynamics of the NP-polymer-gel nanocomposite sponge, which was previously unavailable. Importantly, for the different strain regimes we can clearly demarcate the dominant underlying microscopic phenomenology, which results in the macroscopic stress-strain response of the inorganic sponge.

We emphasize that such inorganic sponge prepared by ice templating are different in morphology and elastic response from materials with large porosity and with an underlying network of interconnected rods or semiflexible polymers. Previous experimental studies have looked at the stress response of a mesh of connected carbon nanotubes of $30 - 40$-nm diameter and lengths spanning several microns [49] prepared by the chemical vapour deposition technique. These system shows three regimes in the stress-strain response, corresponding to (a) bending of nanotubes at low strains, (b) buckling regime at intermediate strains, which shows up as a plateau in the stress-strain curve, and (c) a sharp increase in stress with strain due to relatively dense material with low porosity at strains at greater than 0.6. In contrast, our system has spherical NPs as constituents, which are not amenable to bending at even high strains. Moreover, we show that the walls around the pores do not bend at low strains. Instead, the walls undergo compression maintaining the spherical shape of the voids. However, the walls of our system undergo bending and finally buckling as strains increase beyond 0.05.

Other theoretical models used interconnected networks created by Poisson-Voronoi tessellations and measured stress response by voxel-based finite element methods to show that it effectively captures the stress response of interconnected semi-flexible polymers such as collagen networks [50]. Our system consist of large pores surrounded by percolating walls, where the walls itself have a substructure made of NPs enmeshed in polymers. The response in independent of the composition of the NPs, as it is the response of the polymer mesh, which dominates the elastic behavior at low strains, unlike the systems described by Nachtrab *et al.* [50].

We describe the model in detail in the next section. We present the bulk stress-strain behavior of our model system

in the Sec. III and show that it reproduces the experimental curve to our satisfaction. The three regimes can clearly be demarcated. We then calculate and discuss the reorganization of micro-structure with increasing strains up to 80% as in experiments, before closing with a summary in Sec. IV.

II. MODEL AND METHODS

The macroporous scaffolds used in the experiments comprise walls of densely packed particles enmeshed in cross-linked polymer gel, which surround large open voids. We use non-equilibrium molecular dynamics (MD) as implemented in LAMMPS [51] to realize our model system and use it to study the stress response to applied uni-axial strain by computer simulations. We model the inorganic sponge, i.e., nanoparticles (NPs) trapped in a polymer gel network with large interconnected voids using a coarse grained approach. We omit the polymer degrees of freedom by coarse-graining. A brief overview of how we model the porous scaffolds is given in Fig. 2(a) and its caption, which the reader may refer to before going into details. Since we are modeling a dry aerogel, we do not incorporate viscous effects or include equations for the dynamics of trapped fluid during compression.

1. *Initialization of particle and void positions*: In this step, we place 27 large spheres in a cubic lattice within a cubic simulation box of length L and arrange NPs in an HCP lattice in the space between the spheres. When the large spheres are later removed, spherical open voids remain, which are of the same size as the spheres. Furthermore, the NPs are also considered to be perfect spherical particles (beads) of diameter σ. We chose $\sigma = 22$ nm as was used in the previously reported experiments [41]. Refer to schematic in Fig. 2(a). The unit of length for our simulations is σ. The excluded volume (EV) interactions between NPs are modelled by the purely repulsive WCA (Weeks-Chandler-Anderson) potential [53]. The WCA potential is a modified Lennard Jones potential such that the cut-off of the potential is chosen to be at $r_c = 2^{1/6}\sigma$. The form of the WCA potential is

$$V(r) = 4\epsilon[(\sigma/r)^{12} - (\sigma/r)^6] + F_c r - V_c, \forall\, r < 2^{1/6}\sigma, \quad (1)$$

where F_c and V_c are suitably calculated constants, which ensure that the force and the potential do not have any discontinuity at r_c [53]. Particles were excluded from the spherical regions, which form the voids by suitable WCA repulsive interactions between NPs and the large spheres, which mimic the ice crystals. The lattice constant for the HCP lattice for the initialization of NP positions is chosen to be 1.1σ.

The distance between the centres of adjacent voids were all the same ($L\sigma/3$). The "void particle" diameter is $2R_V$, which is varied to achieve voids of different sizes. This enables us to study systems with different void volume fraction ϕ_V. To realize open connected voids, we chose the value of $2R_V$ to be larger than the distance between the center of voids. The large spheres (representing ice particles) of radius R_V repel the NPs, but we do not implement WCA-repulsion between the ice particles. Thereby the ice particles can overlap. The values of R_V, the initial box size ($L\sigma$), the corresponding initial void volume fraction ϕ_V as well as the initial nominal density ρ_0 used for our study are listed in Table S1 within

(a)

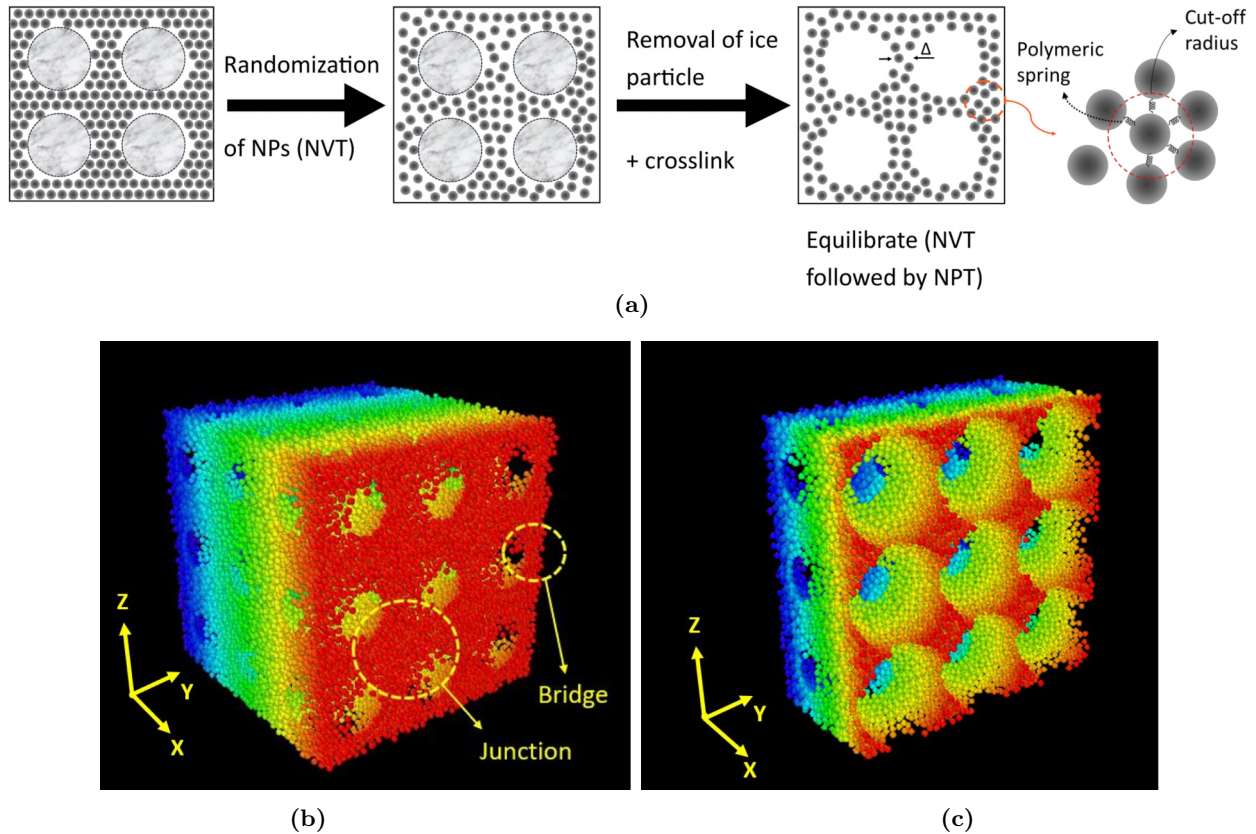**(b)**   **(c)**

FIG. 2. (a) A schematic of how the inorganic sponge is prepared in our simulation model. Left box: The NPs are initialized in a HCP lattice surrounding 27 large (light grey) spheres arranged in a $3 \times 3 \times 3$ cubic lattice where the grey spheres represent the ice-crystal template. We implement excluded volume interaction between the NPs and the large grey spheres. We do not model the polymers in this step. Middle box: The HCP lattice of NPs are melted such that they have liquid like short-range order and surround the large (grey) spheres, which remain fixed in space. Right box: We connect the NPs by springs with neighboring NPs; the spring network mimic the mesh of cross-linked polymers, which hold the NPs in place. Simultaneously the big spheres (which mimic the ice crystals) are removed from the simulation box such that voids remain. The NPs connected by springs (the NPs are enmeshed by the polymer gel in experiments) remain in position surrounding the voids, after which we do NVT and then NPT molecular dynamics simulations to prepare the system before applying uniaxial strain on the scaffold. (b) Snapshots of our cubic box with open voids with $L = 45.45\sigma$ are shown for $\phi_V = 0.55$. Snapshots for $\phi_V = 0.69$ are shown in Fig. S1 of SM [52]. The color gradient is just to aid the eye to distinguish different layers of particles and clearly see the connectivity between voids; one can identify there are 27 interconnected voids with periodic boundary condition implemented. (c) Shows only half of the box along $\hat{x}$ to clearly depict the thickness of the junctions and bridges. The range of the color gradient, from red to blue, now varies over half the box in the $\hat{x}$ direction. The plane $x = L_x/2$ cuts through the middle of the voids.

the Supplemental Material (SM) [52]. The quantity n_{NP} is the number of NPs in the simulation box.

The simulation box size L, as well as values of R_V were simultaneously adjusted to maintain two objectives (*i*) maintain the number density of the NPs in the bridges and junctions as marked in Fig. 2(b), and (*ii*) maintain the minimum bridge thickness $|\Delta/\sigma|$ with approximately the same number of particles in each bridge, where Δ is the minimum bridge thickness between two consecutive junctions. The bridge thickness Δ is shown schematically in Fig. 2(a). The junctions are relatively large aggregates of NPs, and the bridges of NPs connect adjacent junctions. Snapshots from the simulation (after equilibration as described in next step) can be seen in Figs. 2(b) and 2(c) and compared with the SEM images of the experimental system in Fig. 1. In experiments, these clusters of NPs and bridges of NPs at the domain walls are formed during the crystallization of ice crystals and

subsequent cross linking. The large junctions in our model system are a consequence of choosing the spherical voids to be arranged on a lattice for simplicity, while maintaining a minimum value of Δ. In the experimental system we observe the formation of polydisperse voids, whose centers are randomly arranged in space. Therefore, the maximum void fractions of $\phi_V = 0.69$ that we explore in these simulations is less than the experimental void fractions, which can be as high as $\phi_V = 0.9$.

2. Melting the lattice of NPs: We melt the HCP-lattice of NPs before we connect the particles by springs. In this step, we update the position and velocities of NPs in the NVT-ensemble for 50 000 MD steps to melt the lattice. The large spheres play a role similar to that of the ice crystals in experiments. The temperature was chosen to be $T_R = 300$ K and thus the unit of energy chosen for these simulations is $k_B T_R = 1$. The mass M of each NP is chosen

such that the mass density of particles matched that of silica. Thus, $M = 14.8 \times 10^{-21}$ kg for 22-nm beads. The unit of time τ for the MD simulations is thus given by $\tau = \sqrt{M\sigma^2/k_BT_R} = 4.15 \times 10^{-7}$ s. The time step for integration was chosen to be 5 picoseconds (ps), which is $1.2 \times 10^{-5}\tau$. At the end of this step, we obtain random liquid like packing of NPs between "void particles", as they diffuse relatively small distances from their initial positions over 50000 MD steps.

The void-volume fraction ϕ_V for the 27 voids in the simulation box is calculated as $\phi_V = 27V_V/(L\sigma)^3$, where V_V is the volume of the void. To calculate V_V the simulation box can consider to be made up of 27 individual smaller cubes of length $L\sigma/3$, each having a spherical void. Since the diameter of the void is larger than the cube, a part of the sphere overlaps with the adjacent boxes, leading to the connecting voids as observed in the experiment [41]. The void volume is calculated by subtracting the volume of the section outside the smaller cubic box from the volume of the sphere. The list of different values of L used and the radius R_V of bigger spheres, which eventually gives void volume V_V is listed in Table S1 within the SM [52].

3. *Creation of NP mesh*: In this step, the spheres of radius R_V were removed and all NPs whose centers were within the cutoff-distance distance $R_{CL} = 1.5\sigma$ from each other were connected by harmonic springs. The the spring potential is $V_H(r) = \kappa_{CL}(r - r_{ij}^0)^2$, where r_{ij}^0 is the distance between two neighboring NPs i and j at the end of step 2. Each spring represents the effects of cross-linked polymers, which trap the NPs within the mesh of the polymer gel and prevent the NPs from diffusing away [schematically shown in Fig. 2(c)]. In our model, the soft springs maintain the positional constraints effected by the polymer mesh, but at the same time allow the NPs some freedom to move around its mean position. The equilibrium length r_{ij}^0 of the springs is different for each pair of particles but the spring constant $\kappa_{CL} = 100k_BT/\sigma^2$ was chosen to be the same for all springs. The system is then equilibrated in an NVT ensemble.

By altering the value of R_{CL} we can change the mean number of springs N_S in the system. Since a single spring connects two NPs, the number of springs per particle is $(2N_S)/n_{NP}$. It must be noted that the NPs at the interface of the void have different number of springs attached to a particle (N_I) on average, compared to the mean number of springs per particle (N_B) for bulk particles. We identify the particles, which are at the interface by listing the NPs whose centers lie within a spherical shell of radii R_V and $R_V + \sigma$ drawn from the void center. The total number of NPs located at the interface of voids are n_P^I. Table S2 within the SM [52] lists various system characteristics, including the calculated values of N_I, N_B and n_P^I for systems with different values of void fractions to enable the reader to easily compare properties of different systems. We have also carried out calculations with $R_{CL} = 1.25\sigma$ and $R_{CL} = 1.75\sigma$ for the system with $\phi_V = 0.55$, respectively, for which the mean number of spring-connections with its neighbors were $N_B = 6.53$ and $N_B = 13.8$ per NP, respectively. The quantity γ_T in Table S2 within the SM [52] represents the value of strain, which the stress-strain graph transitions to the plateau region; the calculation of this quantity is discussed in the Sec. III.

In Table S2 within the SM [52], we see that as the void fraction ϕ_V increases, the ratio of number of NPs at the interface to the ratio of number of NPs in the junction region changes. While changing ϕ_V, we ensure that Δ remains unchanged, hence we change the box size L as we go to higher ϕ_V. However, this results in larger number of particles at the junctions. Hence the ratio of the number of particles at interface compared to total number of NPs n_P^I/n_{NP} changes nonmonotonically with ϕ_V.

4. *Equilibration in NPT ensemble*: Before measuring the stress response by applying strain in the x direction, we first equilibrated the system using an NVT-ensemble calculation and calculated the equilibrium pressure P_1 of the system for 10^5 iterations. Then fixing the equilibrium pressure to the value P_1, the system was equilibrated in a NPT ensemble.

5. *Applying Strain*: Thereafter, we started applying controlled strain γ in the $\hat{x}$ direction by gradually decreasing the value of L_x, and calculated the σ_{xx} values in the NPT ensemble. The pressure was maintained at P_1 in y, z directions using a Nose-Hoover barostat, such that L_y, L_z could adjust itself at each strain, refer Fig. S2 within SM [52]. The simulation box does not remain cubic any more on compression, and we can calculate the volume of box $V(\gamma) = L_x \times L_y \times L_z$ as strain is applied, and use $V(\gamma)$ to calculate $\rho(\gamma) = Mn_{NP}/V(\gamma)$, which we use later in our analysis. The pressure is calculated using the virial expression for the stress tensor $\sigma_{\alpha\beta}$ for pair of interacting particles i, j, which are separated by $\vec{r}^{ij}$ with force $\vec{f}^{ij}$ is acting between them, viz.,

$$\sigma_{\alpha\beta} = \frac{1}{V}\left(m\sum_i v_\alpha^i v_\beta^i \right) + \frac{1}{2V}\sum_{i,j;i\neq j} r_\alpha^{ij} f_\beta^{ij} \qquad (2)$$

where v is the velocity and the second summation should remind the reader that the summation is over values of particle pairs i, j when $i \neq j$. The indices α, β take the values (x, y, z).

Since we wanted to investigate the effect of compressing the sponge, the strain γ was gradually increased from 0 to 0.8 over 24 million MD time steps (or more for systems with larger void sizes). Thus a sufficiently slow strain rate (1% strain applied in 3×10^5 time steps $\equiv 3.6\tau$) was applied in the simulation to maintain the pseudo-equilibrium. In comparison, note that a harmonic spring with spring constant $\kappa_{CL} = 100k_BT/\sigma^2$ and mass M (equal to that of mass of a NP) has a natural time period of oscillation of only $2\pi\sqrt{M/\kappa_{CL}} \sim \tau$. We measure $x - x$ diagonal component of the stress tensor σ_{xx} as the strain was gradually increased. The Nose-Hoover thermostat was implemented to maintain the temperature of the system and the Nose-Hoover barostat maintained the pressure equal to P_1 in the y and z direction. Thus the corresponding dimensions of the box L_y and L_z fluctuate about its mean value at each γ.

6. *Validation*: Before we commence presenting our results and analysis, we comment on the robustness of our calculations and compare the rates of compression in our simulation to experimental rates. In the x direction a 1000-nm sample was compressed to 200 nm within (at least) 2.4×10^7 time steps, where each MD time step is 5×10^{-12} s. Thus a compression of 0.8 microns was achieved in 1.2×10^{-4} s. This corresponds to a compression rate of ~ 1 cm/s, which is just ten times faster than the experimental rates. To establish that the system
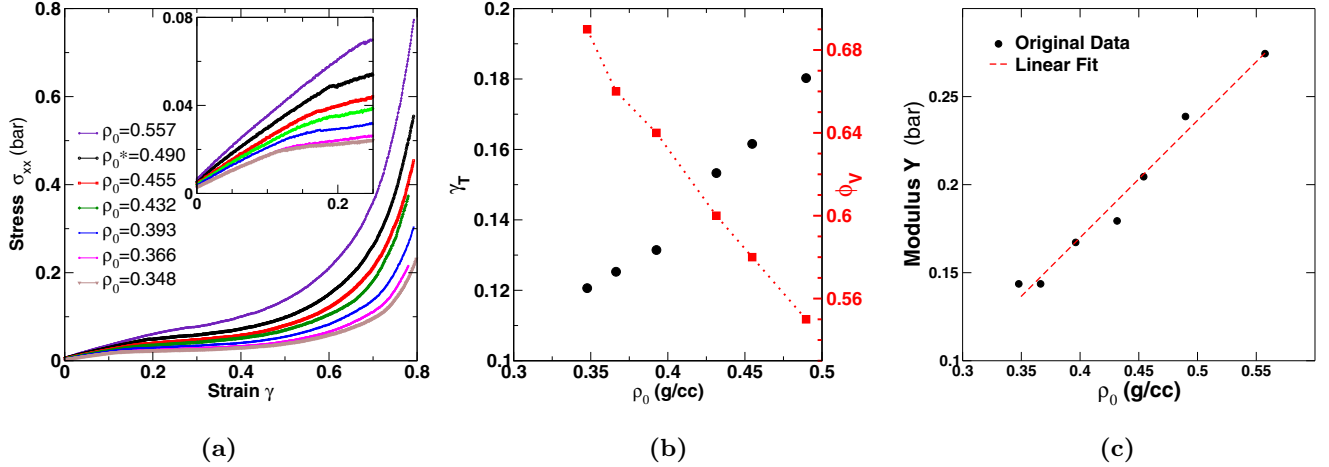
FIG. 3. (a) Response of the system to applied strain by plotting σ_{xx} vs γ for the seven different values of the nominal density ρ_0, in units of g/cc. A decrease in the nominal density corresponds to an increase in the void fraction ϕ_V (at $\gamma = 0$), refer to Table S1 within the SM [52]. We denote $\rho_0 = 0.49$ g/cc as ρ_0^* as we use it later for further analysis. (b) The value of the strain γ_T (at which the transition from the linear to the plateau region occurs) is plotted against the the nominal density ρ_0. The y axis on the right side of the figure shows the void fraction ϕ_V, which is plotted (red symbols) vs ρ_0 on the x axis. Data is for the systems with $R_{CL} = 1.5\,\sigma$. (c) The linear modulus Y is calculated from the stress-strain plots at low strains ($\gamma \to 0$) of (a). Y increases monotonically with the nominal density ρ_0.

is always close to equilibrium during our compression, we compare the $\sigma_{xx} - \gamma$ curve at two other compression rates, viz., three times faster and three times slower than the rate mentioned above. The σ_{xx} versus γ data remain unchanged, independent of this ninefold difference in compression rates, refer the Fig. S3(a) within the SM [52] for the data.

In addition, we created five independent but statistically equivalent systems, to ensure the stress-strain response from straining the five systems are equivalent. Figure S3(b) within the SM [52] shows that the five independent runs yield nearly identical values of stress at each value of strain. The five independent systems are prepared by initializing the velocity by random number generators using different seeds in step 1. This ensures that the NPs are in a different (liquid-like) microstate before the cross linking occurs in step 2. Figures S4, S5, and S6 show snapshots of the void deformations from three independent runs, respectively, for $\phi_V = 0.55$. The reader can confirm that the void deformation is statistically equivalent, and that 27 interconnected open voids are enough to model the system. However, a 3×3 lattice of voids are minimally required in a system with periodic boundary conditions. A 2×2 lattice of voids cannot ensure that each bridge is connected with another independent (nonidentical) bridge of NPs in all directions during deformation.

To show that our system is fully recoverable, we also conducted a compression and expansion study shown in Fig. S3c within the SM [52]. In the compression stage, σ_{xx} increase with increase in γ from 0 to 0.8. We compare this with the stress response when the strain is decreased from 0.8 to 0, during expansion. We do not have viscous dissipation in our modeling of aerogel consequently the stress response during compression and expansion of the system is nearly the same. In reality, one can expect energy loss due to dissipation in the polymers mesh as the NPs move past each other during compression and its release. The small difference in σ_{xx} values at strains beyond $\gamma = 0.5$ is because of the the readjustment of particles over time to minimize energy and release local

constraints in the packed state. Thus σ_{xx} has lower values during expansion. All these additional cross checks give us confidence to present the results from the simulations.

III. RESULTS AND DISCUSSION

In Fig. 3(a) we plot the σ_{xx} component of the pressure tensor as a function of the strain γ for different values of the nominal density ρ_0, or equivalently the void fractions ϕ_V. We can identify three regions in the plot of σ_{xx} versus γ, as strain increases from 0 to 0.8. Before identifying the three regimes in the stress-strain curve and elucidating the physics in detail, we summarize the microscopic picture and origin of the three regimes. In regime-I, the springs connecting the NPs respond to the compression, and the stress increases linearly with strain. In regime-II, the stress enters the plateau regime such that it increases very gradually with strain γ. In this regime the voids get deformed and start collapsing and the box size remains nearly unchanged along $\hat{y}$, $\hat{z}$, i.e., perpendicular to the direction of compression. During deformation of voids and as the NPs enter the void and reorganize themselves, some of the springs (representing polymer elasticity) get stretched whereas other get compressed, though the system gets compressed overall. In regime-III, i.e., for $\gamma > 0.5$, the stress increases rapidly with strain as the voids are filled with particles, and increase of strain leads to large deviation in the lengths of springs. Excluded volume interactions between NPs as they touch each other also contribute significantly towards stress.

A. Stress-strain response

Regime-I: In Fig. 3(a), one first observes a (nearly) linear increase in σ_{xx} with γ for $\gamma \leqslant 0.2$. The extent of the linear region increases with the value of the nominal density $\rho_0 = Mn_{NP}/(L\sigma)^3$; ρ_0 calculated at $\gamma = 0$ for a cubic box, i.e., before the start of compression. The linear increase of σ_{xx} with

γ can be seen in greater detail in the inset of the Fig. 3(a) and we clearly see that the increase in σ_{xx} plateaus off at higher values of γ. In the inset of Fig. 3(a), one can clearly identify the transition from the linear regime (regime-I) to regime-II, which we label as the plateau regime. The value of the strain γ_T at the point of transition from regime-I to regime-II is plotted versus ρ_0 in Fig. 3(b) and tabulated in Table S2 within the SM [52]. To calculate γ_T, we first fit a straight line to the $\sigma_{xx} - \gamma$ curve for $\gamma > 0$ in regime-I. We also fit a straight line to the $\sigma_{xx} - \gamma$ curve in the plateau regime. The intersection of the two straight lines is identified as the transition strain γ_T, for each value of ρ_0. The transition point γ_T increases monotonically with ρ_0. In Fig. 3(b), we also plot the values of the void fraction ϕ_V as we change ρ_0 so that we can clearly correlate the decrease in γ_T with increase in ϕ_V.

From the initial slope (linear regime) of the stress-strain curve shown in Fig. 3(a) we estimate the linear modulus Y of the nanocomposite sponges, which is plotted as a function of ρ_0 in Fig. 3(c). It is known that Y increases linearly with ρ_0 when the dominant elastic response of a porous material is through compaction of the pore walls [41,54]. The porous structure could also respond to stress by bending of the bridges rather than effective compaction of the micro-constituents and in that scenario $Y \sim \rho_0^2$. Thus the functional dependence of Y on ρ_0 can inform us about the microscopic response of the porous scaffold [44].

Our data suggests that $Y \sim \rho$, consistent with experiments [41]. However, we note that in our simulations, ρ_0 is varied over a relatively small range, viz., $\rho_0 = 0.35 - 0.56$, precluding unambiguous confirmation of this scaling. Later in this paper (Sec. III D), we establish by explicitly calculating other microscopic quantities that a linear relation between Y and ρ_0 is reasonable. Contrary to normal expectations, studies at lower densities have higher computational costs, as we must increase the value of L along with R_V to keep the bridge thickness Δ unchanged. Therefore, a larger box has larger number of NPs, which occupy the junctions.

Regime-II (The Plateau regime): Beyond this linear regime, the σ_{xx} versus γ curve in Fig. 3(a) enters the plateau region. Here σ_{xx} increases relatively at a much slower rate with increase in γ than in regime-I, as expected for systems with $\rho_0 > 0.3$ [44]. The relative contributions to the total energy from springs and EV interactions as we compress the system is shown in Fig. S4 within the SM [52]. We establish later in the paper, that in the plateau regime the NPs start entering and occupying the void and the void starts getting deformed. Furthermore, the positions of the NPs get reorganized with respect to each other as they fill up the void. The rate of increase in σ_{xx} with γ is lower for systems with lower ρ_0. This is expected as systems with lower ρ_0 have a larger fraction of particles at the interface of voids and is energetically easy to deform the voids. This plateau regime in the stress-strain curve is consistent with the experimentally observed response seen for the ice-templated sponges [41]. We have observed that the values of L_y and L_z remains relatively unchanged in this regime and start increasing only at strains of larger than 0.5 as the system enters regime-III, refer to Fig. S2 [52]. We also provide simulation movies of the compression mentioned at the beginning of SM [52], which shows the dynamics of void deformation, where we can visually confirm that the

cross-sectional area $L_y \times L_z$ starts changing only later in the simulation (when $\gamma > 0.5$).

Regime-III: As one further increases the compression, the void gets filled with NPs and thereafter, the stress sharply increases with increase in γ. This marks the beginning of the third regime as seen in Fig. 3(a). Systems with lower ρ_0 enter regime-III at higher strains. Measures of box sizes in the transverse direction, L_y, L_z start increasing beyond a certain value of γ, marking the start of regime-III, refer to Fig. S2 within the SM [52]. This implies systems with larger voids can be compressed more before voids get filled up with particles. Figures S4, S5, and S6 within the SM [52] show the void shapes at different values of γ from three independent runs for $\rho_0 = 0.49$ g/cc. We also show snapshots for $\phi_V = 0.69$ system in Fig. S7, confirming that voids fill up at strains $\gamma \geqslant 0.5$. In Fig. S3(b) within the SM [52], we also show for $\rho_0 = 0.49$ g/cc that $\sigma_{xx} - \gamma$ data from 5 independent runs (starting with statistically equivalent but different initial configurations) completely overlap, confirming that the error bars in the value of σ_{xx} are small at the scale of the figures. From the data of $\sigma_{xx} - \gamma$, it is not possible to unambiguously identify the transition point between the second regime to the third regime.

However, the sharp increase in stress only starts for $\gamma > 0.6$ for system with $\rho_0 = 0.49$ g/cc, also because of the significant contributions from the EV repulsion between NPs. At lower values of γ, the contribution to the stress comes primarily from the compression (or elongation) of the harmonic springs connecting NPs, refer to Fig. S8 within the SM [52]. Though the transition point cannot be demarcated clearly from the $\sigma_{xx} - \gamma$ curve, the existence of two different regimes is beyond doubt and is reconfirmed by different behaviours of microscopic quantities in the two regimes. As we show next, the peak of the pair correlation function $g(r)$ decreases with increase of γ in regime-I and regime-II, but height of peak starts increasing beyond $\gamma = 0.5$ for $\rho_0 = 0.49$ g/cc.

B. Microscopic response to applied strain

In Fig. 4(a) we show the pair correlation function $g(r)$ versus distance r between NPs, as we compress along the $\hat{x}$ direction for the system with $\phi_V = 0.55$ (i.e., $\rho_0 = 0.49$ g/cc). The position of the first peak in the pair correlation function shows the highest probability in finding the nearest neighbors of a NP at the corresponding value of r, and the second peak denotes the most probable position to find the next-nearest neighbors from the center of any NP. While the first peak is rather well defined for all values of γ, the second peak of $g(r)$ becomes broader with increasing values of γ. Furthermore, the position of the first peak shifts to smaller values of r with increasing γ; this corresponds to a decrease in the distance between the nearest-neighbor particles.

However, the height of the first peak decreases with increasing γ till $\gamma < 0.5$, after which the peak height again increases as the system enters regime-III, refer inset of Fig. 4(a). This initial decrease corresponds to a wider distribution of distances between a particle and its nearest neighbors, as they occupy the void. For $\gamma > 0.5$, the peaks move further to the left, but the peak height starts to increase as the system becomes more packed. As γ increases from 0 to 0.8 with a
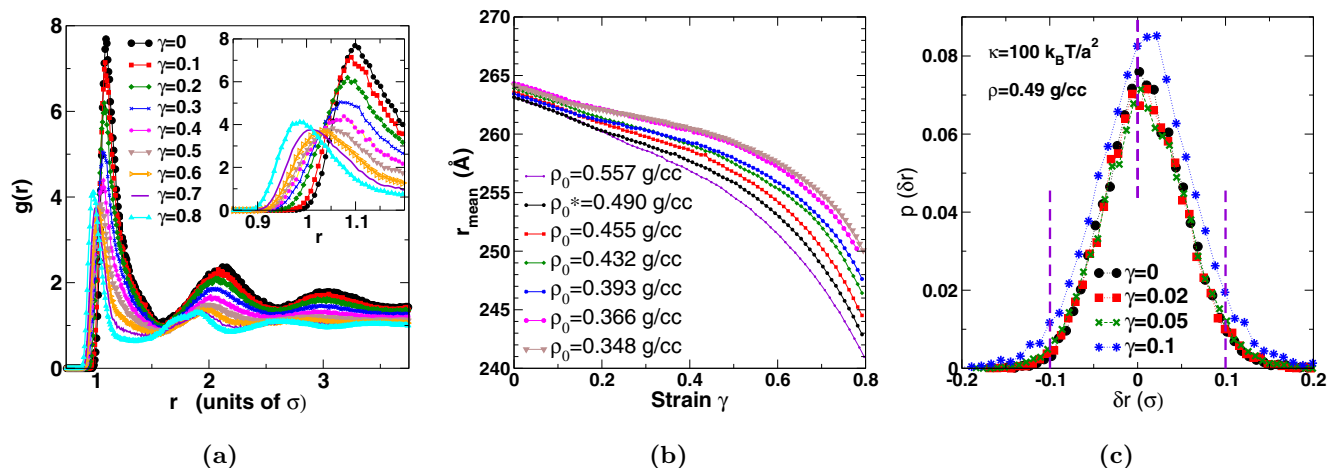
FIG. 4. (a) The pair correlation function $g(r)$ vs distance r from a NP at different values of strains as given in legend, for a system of void fraction $\phi_V = 0.55$ (i.e. $\rho_0 = 0.49$ g/cc) with $R_{CL} = 1.5\,\sigma$. The inset shows the zoomed in $g(r)$ so that the change in the position of the peaks of $g(r)$ can be easily identified. (b) An estimate of the mean distance of the nearest neighbors of a NP r_{mean} (refer to text for calculation details) as function of the strain γ is shown for different ρ_0. (c) Probability distribution $P(\delta r)$ of the deviation of bonds from its mean length vs the deviation δr is shown. The three vertical dashed line at $\delta r = -0.1, 0$, and 0.1 are drawn to help the eye discern the asymmetry in the distribution. On an average the bonds are more extended than compressed. The distributions are normalized: wider distributions also have larger bin size.

volume change of nearly 80% in the sponge, the peak position of $g(r)$ shifts from 1.1σ (24.2 nm) to $\approx\sigma$ (22 nm), i.e., a change of only $\sim10\%$.

Moreover, the second peak of $g(r)$ becomes broader and shifts to the left, as the springs of equilibrium length $\approx 1.4 - 1.5\,\sigma$ get stretched or compressed. The flattening of the second and third peaks with the increase in values of strain γ, points to a loss in long-range correlations in the positions of NPs as they rearrange positions under strain.

Figure 4(b) shows r_{mean} versus γ for different ρ_0 values, where r_{mean} is the mean distance of the nearest neighbors from the center of a NP. The quantity r_{mean} is calculated by first identifying the k neighbors of a given NP by selecting those particles, which are at distances $r_k \leqslant r[g(r)_{\text{min}}]$. The quantity $r[g(r)_{\text{min}}]$ is the position of the first minimum of $g(r)$. We calculate r_{mean} by summing over the values of r_k (for $r_k < r[g(r)_{\text{min}}]$), weighted by the probability of finding a particle at r_k, and then normalize by the area under the curve of the first peak. The area under the peak gives the total number of nearest neighbors surrounding a certain NP. Thus, the quantity r_{mean} gives the mean distance of the nearest-neighbor particles around a NP.

As we see in Fig. 4(b), the r_{mean} value keeps decreasing monotonically with increase in γ; this is further substantiated by the increasing values of harmonic energy term in Fig. S8 [52]. We thus expect that the springs are getting compressed. However, we also observe that as the system transitions from regime-I to regime-II, the rate of decrease of r_{mean} with γ shows an unexpected small upturn beyond $\gamma = 0.2$, especially for systems with lower values of ρ_0. Furthermore, at $\gamma = 0$, we observe that the value of r_{mean} decreases with increasing ϕ_V though we have carefully maintained equivalent densities of NPs in the junctions and bridges before cross linking.

Our attempts to understand these observations led us to unexpected results. Firstly, we plot the probability distribution

$p(\delta r)$ of the fluctuation of the spring length δr about its mean position in Fig. 4(c). We observe that the distribution is asymmetric about $\delta r = 0$, and that a larger fraction of springs are stretched rather than compressed at even $\gamma = 0$. We quantify this by calculating the first moment of this distribution, i.e., δr_{Mean}. For purposes of calculation, the quantity δr is considered positive for stretched springs and considered negative for compressed springs. Moreover, we separately calculate δr_{Mean} for NPs in bulk (B) and for NPs at the interface (I) of voids. We find δr_{Mean} for both to be positive.

The quantity δr_{Mean} versus γ is plotted in Fig. 5(a). In a bulk system without voids, we expect $\delta r_{\text{Mean}} = 0$ for $\gamma = 0$. Moreover, δr_{Mean} initially decreases with increase in γ, reaches a minima at the end of regime-I, and then increases with further increase in γ. This indicates that the springs get more stretched on an average in regime-II, on compressing the system. In regime-II the springs at the interface (on an average) are more stretched than springs at bulk as $\delta r_{\text{Mean}}(I) > \delta r_{\text{Mean}}(B)$. Lastly, the difference between in response of springs at the interface and those at bulk (as measured by δr_{Mean}) increases for systems with larger ϕ_V.

Such observations indicate that the material at the interface of voids are softer and deform more easily on compression as compared to the material in the junctions (bulk of the material). The interface NPs have fewer neighbors (and spring connections) on the side of the void. Hence, at $\gamma = 0$, the interface springs can have larger length fluctuations into the void. We suggest that the interface particles can also easily stretch out and extend into the void due to applied strain, rather than move into the bulk of the material. This creates an asymmetry in the probability distribution of δr, resulting in positive values of δr_{Mean} at all γ values. As seen in Fig. 5(a), systems with lower ρ_0 (corresponding to systems with larger voids and more particles at the interface) exhibit higher values of δr_{Mean} at $\gamma = 0$. We also observe the small differences in
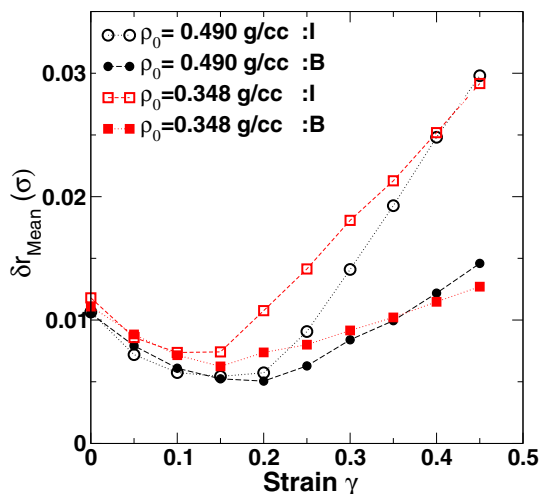
(a)
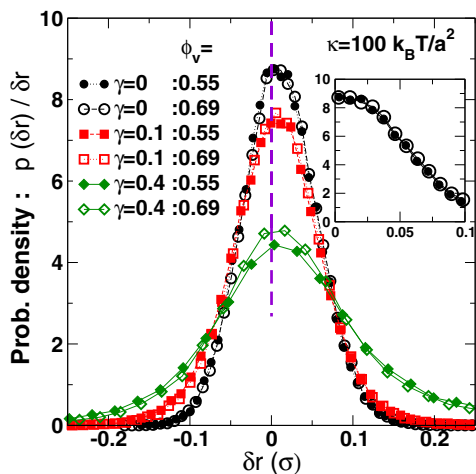
(b)

FIG. 5. (a) The mean deviation of the springs from their equilibrium positions δr_{Mean} is calculated from the probability density distribution of the deviation of springs from their mean position δr (refer to Fig. S9 within the SM [52]) and plotted separately for particles are interface of void (I) and for particles in the bulk (B) against strain γ for two values of ρ_0. In (b), we compare the probability densities of length fluctuations of interface springs for $\phi_V = 0.55$ (filled symbols) and 0.69 (open symbols). The insets are zoomed version of the main figure, for only those data sets, which are indistinguishable in the main plots. The vertical lines at $\delta r = 0$ are guides to the eye.

$p(\delta r)$ for the NPs, which are at the interface and for those. which are in the bulk, in Fig. 5(b) and Fig. S9 within the SM [52].

These small differences in the fluctuations of interface and bulk NPs has consequences for the more discernible differences in the values of $r_{\text{Mean}}(\gamma = 0)$ in Fig. 4(c). The behavior of δr_{Mean} at small γ before the minima and the corresponding change in probability distributions $p(\delta r)/\delta r$ as strain changes from $\gamma = 0$ to $\gamma = 0.1$ confirms effective compression of the springs in regime-I, and confirms conclusion from Fig. 3(c)

that there is a compaction of pore walls at smaller strains. The minima appear at lower strains for systems with lower ρ_0, as the interface can be more easily deformed. Moreover, in Fig. 5(a) we see that $\delta r_{\text{Mean}}(I) > \delta r_{\text{Mean}}(B)$ for $\gamma > 0.2$ in regime-II, confirming the softness of the interface. Finally, as we see in Fig. 5(b) and Fig. S9 within the SM [52], the populations of springs with large $|\delta r|$ (both compression and stretch) increase in regime-II, though δr_{Mean} remains positive. This increase in δr_{Mean} in regime-II explains the small upturn in the rate of fall of r_{mean} beyond $\gamma > 0.2$, which is more discernible for systems with larger voids in Fig. 4.

At the end, we would like to emphasize to the reader, that this system with large open voids is intrinsically very different from a solid system with NPs connected by springs and without any voids, or a solid with very small pores. We would like to emphasise the point that in our system with large open voids, the interfacial particles play a major role in the stress distribution, which leads to these three distinct regimes. In case of a solid system, all particles behave like bulk particles and the number of springs per unit volume are much higher than the porous system. Moreover, the nominal density of the solid system is 1.36 g/cc. The porous system reaches such high density in regime-III at high strain ($\gamma \sim 0.8$). This drastically changes the system response and the results.

However, we believe the system without voids is also quite different from regime-III of the system with voids. The reason is that in the system with voids, there is rearrangement of NPs as the voids collapse as seen in the movies and snapshots of void collapse. Thereby we see that some springs get stretched while others get compressed as the whole system is compressed as a whole. Hence, in regime-III the system with voids will have contributions to the stress from both excluded volume interactions and due contributions from the change in the length of springs. However, on compressing a solid system without voids, there cannot be any major rearrangement of the NP positions with respect to each other in the solid system due to lack of space, and as a consequence, the springs will be primarily compressed as the whole system is compressed, and there is likely negligible contributions from excluded volume interactions to the stress.

Further, we note that effective medium theories [55], in the spirit of Maxwell, cannot capture such functional dependence of the mechanical response of the monolith. Later in the paper (Sec. III D), we show that the response of the nanocomposite sponges can be largely attributed to the NPs at the interface of the voids. This clearly suggests why the response of these sponges cannot be modelled using effective medium theories applicable to random heterogeneous media.

C. Systems with different κ and R_{CL}

We have also studied σ_{xx} versus γ behavior with stiffer ($\kappa = 300 k_B T / \sigma^2$) and softer ($\kappa = 33 k_B T / \sigma^2$) springs, as well as systems with more spring connections per NP (with $R_{CL} = 1.75\sigma$) or fewer ($R_{CL} = 1.25\sigma$). The stress response to applied strain in the x direction for the two cases are plotted in Figs. S10 and S11 within the SM [52], respectively. The corresponding r_{mean}/σ versus γ is also shown to enable the reader to decipher the corresponding changes in microscopic

rearrangement of nearest neighbors as a function of the applied strain. The behavior of r_{mean} versus γ shows behavior consistent with what is described above: Softer systems show a larger upturn of r_{mean} beyond $\gamma \approx 0.2$. Moreover, systems with higher κ or with larger number of spring connections N_B per particle show higher values of σ_{xx} than other systems at the same value of γ, as would be expected. We also have data at different values of ρ_0 at different values of κ and R_{CL}. An increase in κ corresponds to experimental systems where the length of polymer segments between cross links is decreased. Increase in R_{CL} mimics the effect of different cross-link architectures such that there is now a more multiply connected polymer mesh. The effect is more subtle than just an increase in cross-link densities between the polymers, as a simple increase in cross-link density would lead to smaller lengths of polymers (lower κ) between cross links.

We also establish that stress-strain response of the system remains qualitatively unchanged if we introduce smaller voids in the regions, which we refer to as junctions of the sponge. The detail of the effect due to smaller void is described in Sec. III F. However, the transition from regime-I to regime-II shifts to lower values of strain and the transition does not remain as distinct as in systems with voids of uniform size.

D. Characterizing deformation of voids

We now quantify the deformation of the voids as a function of γ. In particular, we investigate whether different voids start deforming and then collapse in a sequential manner, or all of the voids start deforming simultaneously. Furthermore, we can characterize the nature of deformation of the voids in the plateau region. e.g., we can investigate whether with increase in γ, the voids become smaller while maintaining an average spherical shape, or if their shape changes gradually by stretching out in a particular direction while getting compressed in the other directions.

To this end, we calculate geometrical quantities that provide us information about the deformation behavior of the 27 different voids with increase in γ. Firstly, we identify the particles, which make up the void surface by listing all the NPs at the interface. The position of these particles forms a spherical shell with pores (at the points where adjacent voids connect with each other to form open voids) on the surface of each of the shells: refer to Fig. 2 for visualization. We follow the positions of these interface NPs as we strain the systems with different ϕ_V, and we analyze the void deformation characteristics by calculating suitable geometric quantities using the positions of these sets of NP. In particular, we calculate the gyration tensor using the positions of interface particles as γ increases as

$$G_{x,y} = \frac{1}{N} \sum_i r_x^i r_y^i, \qquad (3)$$

where $\vec{r}^i$ is the position of the ith NP from the center of mass of the interface particles for a particular void. Then we diagonalize the matrix to obtain the square root of the ratio of the largest and smallest eigenvalues I_1/I_3. The quantities $(I_1)^2, (I_2)^2, (I_3)^2$ are 3 eigenvalues of the gyration tensor matrix G. We calculate these quantities for each of the 27 voids
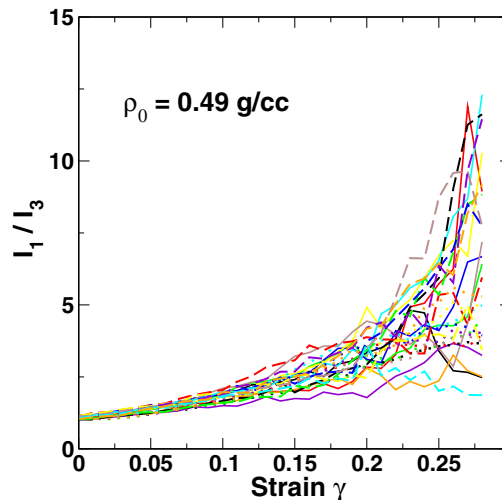
(a)
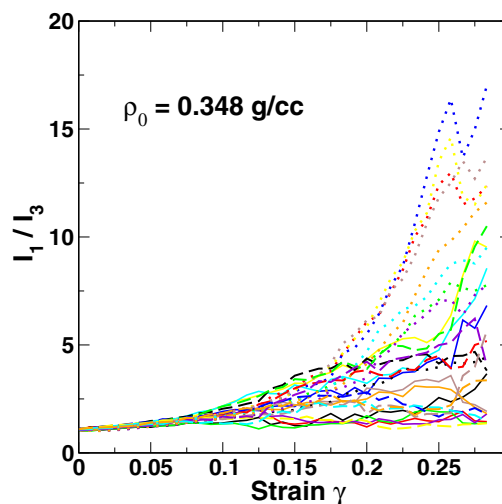
(b)

FIG. 6. The ratio of the largest and the smallest eigenvalues I_1/I_3 of the radius of gyration matrix defined for each of the 27 voids and plotted vs increasing strain γ for (a) $\phi_V = 0.55$ corresponding to $\rho_0 = 0.49$ g/cc and (b) $\phi_V = 0.69$ corresponding to $\rho_0 = 0.348$ g/cc.

separately, and then plot them versus γ to investigate the deformation behavior of each shell.

We follow these quantities only up to $\gamma = 0.3$. Beyond this value of γ, we have observed in simulation movies of the deformation (refer to SM [52]) that the voids interpenetrate and it is no longer meaningful to calculate the above mentioned quantities using NPs, which identify the interface. We present I_1/I_3 for each of the 27 different voids for the system for two different values of ϕ_v, viz $\phi_v = 55\%$ and $\phi_V = 69\%$ for the $R_{CL} = 1.5\,\sigma$ system in Fig. 6.

The major conclusions from Fig. 6 for two values of ρ (or equivalently ϕ_V) can be summarized as follows:

(i) Up to a strain of nearly 3% (or less), the ratio I_1/I_3 remains very close to 1 for all of the voids, indicating that

there is no substantial change in shape of the voids in the entire scaffold. This basically corresponds to the first linear regime in the stress strain curve. All the increase in stress in primarily due to the compression of springs but the NPs have moved only slightly from their equilibrium positions and scaffold maintains its shape. This is consistent with our assertion that the initial linear response of the system is obtained by compression of the sponge walls, and thus $Y \sim \rho$. We further calculate and show the quantity asphericity A_s in Fig. S12 within the SM [52], which is a measure of the deviation in shape from the perfect sphere. One can notice that even at $\gamma = 0$, some of the voids have nonzero values of asphericity, which in turn depends on the arrangement and identification of interface particles around the open voids. The quantity A_s remains close to zero for small deformations.

(ii) At higher strains, i.e., $4 - 12\%$, there is mild deformation of the scaffold structure, such that I_1/I_3 increases to around 2 at the end of the range of γ mentioned. There is also a slight spread in the values of I_1/I_3, which indicates that each void deforms a bit differently though the basic shape of the voids is still maintained. However, we know that the deformation is nonaffine, as we know that the NPs readjust their positions such that some springs are stretched while others are more compressed with respect to their equilibrium lengths.

(iii) As the system enters the plateau region of the stress strain curve, each void deforms in its own different manner. Some of the voids stretch out to take highly asymmetrical shapes. Some other voids deform significantly at intermediate values of γ to become asymmetrical, but at still higher deformations I_1/I_3 again becomes ≈ 1 as the void fills up. This can be confirmed in the simulation movies listed in SM [52]. This could be because all the eight junctions surrounding a particular void close in on the void as the neighboring voids deform, and thereby the NPs in junctions rearrange their positions with respect to each other. Also, the values of I_1/I_3 change in a arbitrary manner, such that some values increase significantly, some stay close to value 2, and others first increase and then decrease (or stay constant). Finally at 28% strain, one has the entire range of all possible values from 1 to 16 for both $\phi_V = 0.55$ and $\phi_V = 0.69$. Thus for $\gamma > 0.12$ each void simultaneously undergoes large deformations, and each deformation in shape follows a stochastic path.

E. Scaling with density change $\Delta \rho$

At $\gamma = 0$, we expect the stress $\sigma_{xx}(\gamma = 0)$, with dimensions of energy density, to depend on the number of particles in the simulation box as well as the number of spring-connections per particle as determined by R_{CL}. As we increase ϕ_V, ρ_0 decreases as does the number density of springs, leading to proportional decrease in the energy density. The number density of springs in the bulk (regions without voids) should increase as ρ_{NP}^2, where ρ_{NP} is the number density of NPs. This is because the number of springs in a certain volume will increase as one increases the number of particles in the volume, as well as number of neighbors of the particles in the volume. However, the number of particles at the interface increases as a consequence the lowering of ρ_0 and since interface particles have fewer connections, the energy density (at zero strain) will

decrease as $\sim (\rho_0)^n$ with $n > 1$. Increase in interface area can also affect the stress response at finite strains as we know that interface particles deviate more from their mean position as compared to NPs away from it.

As the sample is compressed, γ increases and correspondingly, σ_{xx} increases. The increase in γ results in a change in the box volume. We define the instantaneous average nominal density of the simulation box as $\rho(\gamma) = \rho = M N_{NP}/V[\gamma]$. With increase in γ, there is an increase in ρ, starting from ρ_0 at $\gamma = 0$. In the plateau regime, the L_y and L_z remain unchanged to keep Poisson ratio very close to zero, and thus density ρ_γ increases linearly with γ. We define the instantaneous (strain dependent) increase in monolith nominal density above that of the prepared state as $\Delta \rho = \rho - \rho_0$. With compression, there is an increase in $\Delta \rho$ and in σ_{xx}.

In elastic foams, the transition to the plateau region is associated with the onset of buckling and ingress of the walls into the voids, while the increase in stress at high strain is associated with impingement of pore walls. We conjecture that the stress developed during compression after the transition to the plateau region would depend on the instantaneous increase in monolith nominal density $\Delta \rho$. We observe that the stress (after the transition to the plateau and, scaled by an arbitrary multiplicative factor, $F_{\rho_0} \sigma_{xx}$) appears to have a universal response as a function of $\Delta \rho$ as seen Fig. 7(a) for monoliths at 6 different values of ρ_0. Such universal scaling is observed for each of the three values of κ as seen in Fig. 7(a).

Furthermore, if we vary the number of spring connections per particle by changing R_{CL}, then we again see universal behavior as seen in Fig. 7(b) shows data for $N_B = 6.53$, 10.2, and 13.8. In the insets in Fig. 7, we plot the vertical scale factor F_{ρ_0} as a function of ρ_0 and observe that F_{ρ_0} decreases with ρ_0. The values of F_{ρ_0} used is also listed in Tables of S3 and S4 within the SM [52]. We present this as an interesting observation that holds for our model, even when the spring constant is changed, or the interaction range is varied. *A priori*, we did not expect to find universal behavior, especially since the different stress-strain regimes correspond to different underlying physics. However, data suggests that the number of spring connections at zero strain at a particular ρ_0 determines the sponges stress-strain behavior over the entire range of γ considered. A better understanding of the physical origin of the scale factor, and its dependence on ρ_0 needs further study.

F. Different lattice structure of voids

To ensure that a polydispersity in the size of voids does not significantly modify the basic conclusions of our paper, we have also done a preliminary study of the stress-strain response of a system with voids of two different sizes. To that end, we have added additional data for the stress-strain response in a modified system, where we introduce small voids of radius 3.5σ in the regions, which we labeled junctions in the (previous) $\phi_V = 0.55$ system. Thus, the arrangement of the voids now BCC lattice structure (or more accurately called the CsCl lattice structure as the newly created voids in the junctions are smaller in size than the other voids), and the void fraction in the modified system is $\phi_V = 0.606$. Snapshots of this modified system can be seen in Fig. S13 within the SM [52]. The snapshots show the system before strain is applied.
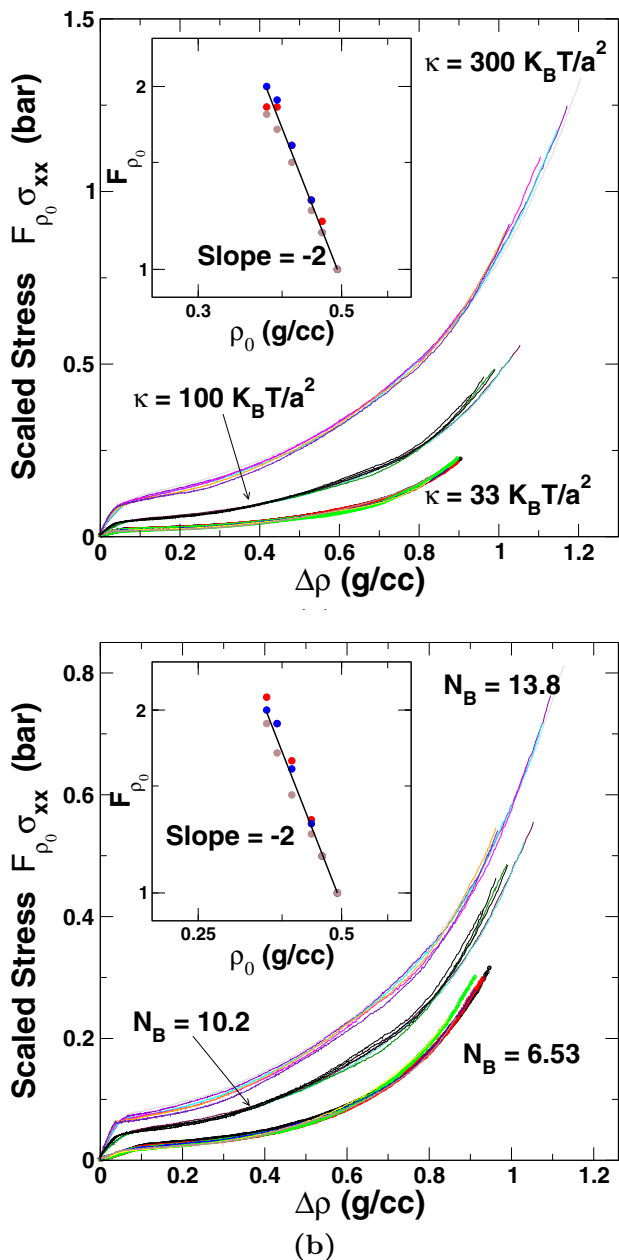
FIG. 7. (a) The scaled stress $F_{\rho_0}\sigma_{xx}$ vs the strain dependent increase in nominal density $\Delta\rho = (\rho[\gamma] - \rho_0)$. We calculate $\rho(\gamma)$ by calculating the ratio of the mass of all the particles MN_{NP} and the volume of the box at different values of strain γ. Box volume $V[\gamma]$ adjusts itself with increasing γ as $L_x \times L_y \times L_z\sigma^3$. Data for different values of ρ_0 overlaps perfectly for (a) each of the 3 different values of κ and (b) each of the 3 different values of N_B. In each subfigure, the inset shows the vertical scale factor F_{ρ_0} as a function of ρ_0. In the inset, the scaling factor F_{ρ_0} is plotted versus ρ_0 with the log scale on both axes: symbols indicated in red, blue, and grey symbols correspond to (a) $\kappa = 33k_BT/\sigma^2$, $100k_BT/\sigma^2$ and $300k_BT/\sigma^2$ and (b) $N_B = 6.53$, 10.2, and 13.8, respectively. The slope of the line is -2. We have a rather small range of ρ_0 considered, thereby we do not claim a scaling law of $F_{\rho_0} \sim (\rho_0)^2$. In the insets, some symbols overlap and hence appear invisible. Values of F_{ρ_0} are given in Tables S3 and S4 within the SM [52].

In Fig. S14, we see a broad qualitative similarity of the stress-strain data in this modified system with the counterpart system with voids arranged in cubic lattice. We have plotted the data of the unmodified system along with the stress-strain response of the system with BCC lattice of voids, to enable direct comparison of data. But, if we investigate in detail, we observe the nature of three regimes gets altered due to the introduction of a secondary void with different size. Firstly, we see a much more gradual transition between regime-I and regime-II. Upon further investigation we find that the smaller voids start deforming much at much lower values of γ, as compared to the larger voids. We can see this in the data of I_1/I_3 and the asphericity, presented in Fig. S14 comparing the deformation in larger and smaller voids of the BCC system. Due to smaller bridge thickness (Δ) around the small void, γ_T is less for BCC system. Such behavior is also observed for experimental system with polydisperse void size and systems with anisotropic void shape. Also, the smaller void diameter leads to faster collapse of the entire void, which leads to sharper upturn in regime-III.

However, a systematic analysis of polydisperse voids, or voids arranged in different lattice structures, e.g., FCC, hexagonal or other lattice, will be reported in the future.

IV. SUMMARY

The elastic stress-strain response of an ice-templated polymer nanocomposite aerogel is well represented by our coarse grained model system where the cross-linked polymer matrix enmeshing the NPs is represented as springs connecting the nanoparticles. This model for a monolith with open, interconnected voids qualitatively reproduces the experimental results reported in the literature. Since we do not know the length of polymer segments between cross links as well as the distribution of lengths between cross links, we use an identical of κ for all springs connecting the NPs. We establish that choice of different κ values do not qualitatively change the stress strain response of the system. In our simulations, the system modulus is primarily determined by stretching or compression of the springs connecting the nanoparticles.

From the deformation analysis of the voids, we observe that the voids remain nearly spherical till $\approx 12\%$ strain. Beyond this, each of the voids get deformed in a stochastic manner. Our simulations are consistent with experimental observations that the low-strain linear response arises from compression of the pore walls.

Over and above establishing that a simple coarse-grained microscopic approach is able to reproduce the elastic response of such a multiscale system, we have been able to provide new insights:

(i) As the void collapse, some of the springs get stretched, though others are compressed during compression of the porous system.

(ii) At zero strain, the distribution of deviations from the mean length of springs is asymmetric. On an average the springs stretch out due to thermal fluctuations rather than get compressed. The fluctuation of interface springs are quantitatively different from those situated at the junctions.

(iii) When the system is compressed, the springs at the interface tend to show larger deviations from mean length

as compared to springs, which are located away from the interface. The quantitative difference increases for systems with larger void fractions.

(iv) Our results indicate that interface properties significantly affect the transition to the plateau regime.

(v) We report an unexpected collapse of the stress σ_{xx} versus $\Delta\rho$ when σ_{xx} is scaled a factor F_{ρ_0}, which decreases with the increase in nominal density. This data collapse on scaling by factor F_{ρ_0} holds true for the entire range of nominal densities studied for different values of κ and R_{CL}. An unambiguous understanding of this collapse is lacking at this time.

Thus, we conclude that the coarse-grained microscopic model is able to reproduce the elastic response of inorganic sponges as seen experimentally, in spite of the simplification of replacing cross-linked polymers by springs. In addition, we obtained insights from the microscopic model, which we hope will spawn further studies and analysis in future.

This study can be extended in many directions, some of which we plan to carry out in the future. In particular we have ignored the stochasticity in the size of voids and considered all spring to be harmonic springs. Furthermore,

we have considered a cubic lattice of spherical voids. While a study with voids in a *CsCl* lattice, reminiscent of a BCC lattice, seem to indicate that the qualitative response remains similar as that with cubic lattice, we expect that cuboid voids with very many particles at the interface could show significant differences with the current study. In addition, if one had semiflexible polymers instead of the flexible polymers considered here, it is not obvious that we can replace the effect of cross links between semiflexible polymers by harmonic springs. Furthermore, for liquid filled sponges the hydrodynamic effects of squeezing out fluid have not incorporated as of yet [56]. We plan to first extend this study by replacing the spherical nanoparticles by rod like particles, and considering nonspherical voids in the recent future.

[1] S. K. Kumar and R. Krishnamoorti, Nanocomposites: Structure, phase behavior, and properties, Ann. Rev. Chem. Biomolecular Eng. **1**, 37 (2010).

[2] M. Moniruzzaman and K. I. Winey, Polymer nanocomposites containing carbon nanotubes, Macromolecules **39**, 5194 (2006).

[3] H. Kim, A. A. Abdala, and C. W. Macosko, Graphene/polymer nanocomposites, Macromolecules **43**, 6515 (2010).

[4] A. J. Crosby and J.-Y. Lee, Polymer nanocomposites: The "nano" effect on mechanical properties, Polym. Rev. **47**, 217 (2007).

[5] M. Safdari and M. S. Al-Haik, A review on polymeric nanocomposites, in *Carbon-Based Polymer Nanocomposites for Environmental and Energy Applications* (Elsevier, Amsterdam, 2018), p. 113.

[6] B. L. Smith, T. E. Schäffer, M. Viani, J. B. Thompson, N. A. Frederick, J. Kindt, A. Belcher, G. D. Stucky, D. E. Morse, and P. K. Hansma, Molecular mechanistic origin of the toughness of natural adhesives, fibres and composites, Nature (London) **399**, 761 (1999).

[7] P. Podsiadlo, A. K. Kaushik, E. M. Arruda, A. M. Waas, B. S. Shim, J. Xu, H. Nandivada, B. G. Pumplin, J. Lahann, A. Ramamoorthy, and N. A. Kotov, Ultrastrong and stiff layered polymer nanocomposites, Science **318**, 80 (2007).

[8] S. Deville, Freezing as a path to build complex composites, Science **311**, 515 (2006).

[9] E. Senses, M. Tyagi, M. Pasco, and A. Faraone, Dynamics of architecturally engineered all-polymer nanocomposites, ACS Nano **12**, 10807 (2018).

[10] J.-G. Park, J. D. Forster, and E. R. Dufresne, High-yield synthesis of monodisperse dumbbell-shaped polymer nanoparticles, J. Am. Chem. Soc. **132**, 5960 (2010).

[11] J. R. Capadona, O. Van Den Berg, L. A. Capadona, M. Schroeter, S. J. Rowan, D. J. Tyler, and C. Weder, A versatile approach for the processing of polymer nanocomposites with self-assembled nanofibre templates, Nat. Nanotechnol. **2**, 765 (2007).

[12] B. Lowe, J. G. Hardy, and L. J. Walsh, Optimizing nanohydroxyapatite nanocomposites for bone tissue engineering, ACS Omega **5**, 1 (2020).

[13] M. C. Fernandes, J. Aizenberg, J. C. Weaver, and K. Bertoldi, Mechanically robust lattices inspired by deep-sea glass sponges, Nat. Mater. **20**, 237 (2020).

[14] Q. Zhang, H. Lu, N. Kawazoe, and G. Chen, Pore size effect of collagen scaffolds on cartilage regeneration, Acta Biomaterialia **10**, 2005 (2014).

[15] B. Sitharaman, Nanoscale probes for the imaging of RNA in living cells, in *Nanobiomaterials Handbook* (CRC Press, Boca Raton, FL, 2016), p. 499.

[16] S. K. Kumar, V. Ganesan, and R. A. Riggleman, Perspective: Outstanding theoretical questions in polymer-nanoparticle hybrids, J. Chem. Phys. **147**, 020901 (2017).

[17] R. A. Riggleman, G. Toepperwein, G. J. Papakonstantopoulos, J.-L. Barrat, and J. J. de Pablo, Entanglement network in nanoparticle reinforced polymers, J. Chem. Phys. **130**, 244903 (2009).

[18] H. Kang, F. A. Detcheverry, A. N. Mangham, M. P. Stoykovich, K. C. Daoulas, R. J. Hamers, M. Müller, J. J. de Pablo, and P. F. Nealey, Hierarchical Assembly of Nanoparticle Superstructures from Block Copolymer-Nanoparticle Composites, Phys. Rev. Lett. **100**, 148303 (2008).

[19] K. C. Daoulas, M. Müller, M. P. Stoykovich, S.-M. Park, Y. J. Papakonstantopoulos, J. J. de Pablo, P. F. Nealey, and H. H. Solak, Fabrication of Complex Three-Dimensional Nanostructures from Self-Assembling Block Copolymer Materials on Two-Dimensional Chemically Patterned Templates with Mismatched Symmetry, Phys. Rev. Lett. **96**, 036104 (2006).

[20] I. Pastoriza-Santos, C. Kinnear, J. Pérez-Juste, P. Mulvaney, and L. M. Liz-Marzán, Plasmonic polymer nanocomposites, Nat. Rev. Mater. **3**, 375 (2018).

[21] S. Mubeena and A. Chatterji, Hierarchical self-assembly: Self-organized nanostructures in a nematically ordered matrix of

self-assembled polymeric chains, Phys. Rev. E **91**, 032602 (2015).

[22] S. Mubeena and A. Chatterji, Hierarchical and synergistic self-assembly in composites of model wormlike micellar-polymers and nanoparticles results in nanostructures with diverse morphologies, European Phys. J. E **42** (2019).

[23] A. C. Balazs, T. Emrick, and T. P. Russell, Nanoparticle polymer composites: Where two small worlds meet, Science **314**, 1107 (2006).

[24] M. Laurati, G. Petekidis, N. Koumakis, F. Cardinaux, A. B. Schofield, J. M. Brader, M. Fuchs, and S. U. Egelhaaf, Structure, dynamics, and rheology of colloid-polymer mixtures: From liquids to gels, J. Chem. Phys. **130**, 134907 (2009).

[25] M. Wyart, H. Liang, A. Kabla, and L. Mahadevan, Elasticity of Floppy and Stiff Random Networks, Phys. Rev. Lett. **101** (2008).

[26] J. P. Randall, M. A. B. Meador, and S. C. Jana, Tailoring mechanical properties of aerogels for aerospace applications, ACS Appl. Mater. Interfaces **3**, 613 (2011).

[27] K. Davami, L. Zhao, E. Lu, J. Cortes, C. Lin, D. E. Lilley, P. K. Purohit, and I. Bargatin, Ultralight shape-recovering plate mechanical metamaterials, Nat. Commun. **6**, 10019 (2015).

[28] L. R. Meza, S. Das, and J. R. Greer, Strong, lightweight, and recoverable three-dimensional ceramic nanolattices, Science **345**, 1322 (2014).

[29] H.-S. Ma, J.-H. Prévost, R. Jullien, and G. W. Scherer, Computer simulation of mechanical structure–property relationship of aerogels, J. Non-Cryst. Solids **285**, 216 (2001).

[30] T. A. Schaedler, A. J. Jacobsen, A. Torrents, A. E. Sorensen, J. Lian, J. R. Greer, L. Valdevit, and W. B. Carter, Ultralight metallic microlattices, Science **334**, 962 (2011).

[31] N. A. Fleck, V. S. Deshpande, and M. F. Ashby, Micro-architectured materials: Past, present and future, Proc. R. Soc. A **466**, 2495 (2010).

[32] S. Deville, *Freezing Colloids: Observations, Principles, Control, and Use* (Springer International Publishing, New York, 2017).

[33] S. Deville, The lure of ice-templating: Recent trends and opportunities for porous materials, Scr. Mater. **147**, 119 (2018).

[34] C.-Y. Hsieh, S.-P. Tsai, M.-H. Ho, D.-M. Wang, C.-E, Liu, C.-H. Hsieh, H.-C. Tseng, and H.-J. Hsieh, Analysis of freeze-gelation and cross-linking processes for preparing porous chitosan scaffolds, Carbohydr. Polym. **67**, 124 (2007).

[35] M. C. Gutiérrez, M. L. Ferrer, and F. del Monte, Ice-templated materials: Sophisticated structures exhibiting enhanced functionalities obtained after unidirectional freezing and ice-segregation-induced self-assembly, Chem. Mater. **20**, 634 (2008).

[36] S. Chatterjee, K. Shanmuganathan, and G. Kumaraswamy, Fire-retardant, self-extinguishing inorganic/polymer composite memory foams, ACS Appl. Mater. Interfaces **9**, 44864 (2017).

[37] S. Chatterjee, P. Doshi, and G. Kumaraswamy, Capillary uptake in macroporous compressible sponges, Soft Matter **13**, 5731 (2017).

[38] S. Chatterjee, A. Potdar, S. Kuhn, and G. Kumaraswamy, Preparation of macroporous scaffolds with holes in pore walls and pressure driven flows through them, RSC Adv. **8**, 24731 (2018).

[39] C. Das, S. Chatterjee, G. Kumaraswamy, and K. Krishnamoorthy, Elastic compressible energy storage devices from ice templated polymer gels treated with polyphenols, J. Phys. Chem. C **121**, 3270 (2017).

[40] B. Pandey, S. Chatterjee, N. Parekh, P. Yadav, A. Nisal, and S. S. Gupta, Silk-mesoporous silica-based hybrid macroporous scaffolds using ice-templating method: Mechanical, release, and biological studies, ACS Appl. Bio Mater. **1**, 2082 (2018).

[41] R. Rajamanickam, S. Kumari, D. Kumar, S. Ghosh, J. C. Kim, G. Tae, S. S. Gupta, and G. Kumaraswamy, Soft colloidal scaffolds capable of elastic recovery after large compressive strains, Chem. Mater. **26**, 5161 (2014).

[42] G. Li, Z. Liu, Q. Huang, Y. Gao, M. Regula, D. Wang, L.-Q. Chen, and D. Wang, Stable metal battery anodes enabled by polyethylenimine sponge hosts by way of electrokinetic effects, Nat. Energy **3**, 1076 (2018).

[43] K. Suresh, A. Chowdhury, S. K. Kumar, and G. Kumaraswamy, Critical role of processing on the mechanical properties of cross-linked highly loaded nanocomposites, Macromolecules **52**, 5955 (2019).

[44] L. J. Gibson and M. F. Ashby, *Cellular Solids* (Cambridge University Press, Cambridge, 1997).

[45] J. Zhao, L. Wu, C. Zhan, Q. Shao, Z. Guo, and L. Zhang, Overview of polymer nanocomposites: Computer simulation understanding of physical properties, Polymer **133**, 272 (2017).

[46] G. G. Vogiatzis, E. Voyiatzis, and D. N. Theodorou, Monte carlo simulations of a coarse grained model for an athermal all-polystyrene nanocomposite system, Eur. Polym. J. **47**, 699 (2011).

[47] P. Khan and G. Goel, Martini coarse-grained model for clay–polymer nanocomposites, J. Phys. Chem. B **123**, 9011 (2019).

[48] J. J. de Pablo, Coarse-grained simulations of macromolecules: From DNA to nanocomposites, Annu. Rev. Phys. Chem. **62**, 555 (2011).

[49] Z. Dai, L. Liu, X. Qi, J. Kuang, Y. Wei, H. Zhu, and Z. Zhang, Three-dimensional sponges with super mechanical stability: Harnessing true elasticity of individual carbon nanotubes in macroscopic architectures, Sci. Rep. **6**, 18930 (2016).

[50] S. Nachtrab, S. C. Kapfer, C. H. Arns, M. Madadi, K. Mecke, and G. E. Schröder-Turk, Morphology and linear-elastic moduli of random network solids, Adv. Mater. **23**, 2633 (2011).

[51] S. Plimpton, Fast parallel algorithms for short-range molecular dynamics, J. Comput. Phys. **117**, 1 (1995).

[52] See Supplemental Material at http://link.aps.org/supplemental/10.1103/PhysRevMaterials.6.025604 for simulation movie files of compression of the simulation box with 27 voids and a movie of deformation of an individual void; Tables containing the parameters for the simulation and data analysis; Snapshots of systems with different void fractions for different values of applied strain; Data on box length versus strain in y and z direction; Figures for validation and robustness of our simulation; Spring energy density and excluded volume interaction energy density as function of strain; Effect of varying spring constant and cross-link density; Figure indicating variation in asphericity of voids with increasing strain; Snapshot of a BCC configuration of voids in simulation; Stress-strain data on the compression of a nano-composite system with BCC arrangement of voids.

[53] M. P. Allen and D. J. Tildesley, *Computer Simulation of Liquids* (Clarendon Press, Oxford, 1987).

[54] G. Kumaraswamy, K. Suresh, H. Lama, M. G. Basavaraj, and D. K. Satapathy, Ice templated nanocomposites containing rod-like hematite particles: Interplay between particle anisotropy and particle–matrix interactions, J. Appl. Phys. **128**, 034702 (2020).

[55] S. Torquato, *Random Heterogeneous Materials* (Springer, New York, 2002).

[56] J. L. B. de Araújo, J. S. de Sousa, W. P. Ferreira, and C. L. N. Oliveira, Viscoelastic multiscaling in immersed networks, Phys. Rev. Research **2**, 033222 (2020).